Experimental study on developing in-situ hierarchical micro/nanocrystals for improved capillary wicking

Xiao Yuan[1], Yanping Du[1,2,*], Guochao Fei[1], Ruijie Yang[1], Chao Wang[3], Qian Xu[4], Chuan Li[5]

[1]China-UK Low Carbon College, Shanghai Jiao Tong University, Shanghai, 201306, China

[2]Department of Engineering, Faculty of Environment, Science and Economy, University of Exeter, Penryn Campus, Penryn, Cornwall TR10 9FE, United Kingdom

[3] Guangdong Provincial Key Laboratory on Functional Soft Condensed Matter, School of Materials and Energy, Guangdong University of Technology, Guangzhou 510006, China

[4]School of Energy and Environmental Engineering, Shunde Graduate School, University of Science and Technology Beijing, Beijing, 100083, China

[5]MOE Key Laboratory of Enhanced Heat Transfer and Energy Conservation, Beijing Key Laboratory of Heat Transfer and Energy Conversion, Beijing University of Technology, Beijing, 100124, China

* Correspondence: yanping.du@sjtu.edu.cn; y.du2@exeter.ac.uk

Abstract: The superior capillary wicking capability of hierarchical surfaces determined by the capillary pressure and viscous resistance plays a critical role in developing the high-efficient thermal management devices. In this study, a novel chemical oxide method for fabricating the in-situ micro/nanocrystal structures on the Cu substrates with prominently improved capillary wicking capability is proposed. Single scaled and hierarchical structures can be fabricated, and the capillary wicking capability of the hierarchical structures exhibits the much higher wicking coefficient than that of the single scaled structures. The wicking coefficient on the nanosheet and micro-flowers (NSMF) hierarchical surface was measured as 3.77 $mm/s^{0.5}$, which indicates a maximum improvement of 146.4 % compared to single scaled structures. NSMF structure can provide two-tier pores for strengthening the capillary pressure driven by the nanoscale pores and reducing the viscous resistance driven by the micro pores. It is worth noting that the ultrafast wicking on the hierarchical surface is useful in creating extremely effective thermal management systems and advanced heat exchangers.

Keywords: Capillary wicking; In-situ micro/nanocrystals; Hierarchical structure; Liquid circulation; Surface morphology

Nomenclature		*Abbreviations*	
l	wicking distance, [mm]	NG	nanograss
P_{cap}	capillary pressure	NGMP	nanograss and micro-petals
K	permeability	NGMF	nanograss and micro-flowers
t_t	time, [s]	NSMF	nanosheets and micro-flowers
W	wicking coefficient, [mm/s$^{0.5}$]	*Greek symbols*	
R_f	dynamic liquid wicking front, [mm]	σ	surface tension, [N/m]
R_c	contact line, [mm]	θ	contact angle
R_t	inner diameter, [mm]	μ	viscosity
$V_{initial}$	initial volume of water, [μL]	δ	thickness
$H_{initial}$	initial height of water, [mm]	ε	porosity
F_{cap}	capillary force		
$F_{friction}$	frictional force		
$R_{geometry}$	geometry curvature of the liquid		
A_{area}	cross-sectional area		
C_1	empirical constant		
C_2	empirical constant		
B_1	empirical constant		
P	perimeter of dynamic wicking liquid front		

1. Introduction

Capillary wicking on the hierarchical micro/nano structures which has been used in the numerous promising applications including thermal management [1-10], microfluidics [11-17] and water harvesting [18-22] has attracted significant attention. Due to the microelectronic devices with miniaturization and integration, efficient thermal management with a high heat flux removal in limited dissipation space becomes a big issue that need to be resolved. Boiling heat transfer with huge latent heat is a promising approach for solving the above-mentioned difficulty. It is important that the liquid replenishing is a crucial factor that determines the enhancement of the thermal performance. Therefore, wicking structures has been used to promote the boiling heat transfer, which can maintain the heated surface wet at ultra-high heat flux due to the wicking liquid for replenishing to the dry-out space, delaying the occurrence of heat transfer deterioration and the critical heat flux (CHF) [23-27].

Wicking is the term used to describe the spreading of droplets or propagation of

liquid in a thin film under the influence of capillary pressure, which has been shown to be strongly correlated with surface morphology and roughness [28]. Until now, three categories of wicking structures have been studied: microscale structures, nanoscale structures and hierarchical micro/nano structures. As stated, the capillary wicking performance of the wicking structures with a single length scale is determined by the capillary pressure to viscous resistance ratio. The wicking microstructures, including microchannels [29-33], micropillars [34-43], micropores [44-46] possess the high permeability but low capillary pressure due to the large length scale pores. To investigate the dynamics of microscale liquid propagation in micropillar arrays, Alhosani et. al [39] discovered that the ration of pillar height to edge-to-edge spacing has a substantial impact on the microscopic motion of the liquid front. When compared to wicks made of single meshes, Chen et. al [46] discovered that a multilayer composite micromesh wick with coarse and fine meshes demonstrates a considerable improvement in wicking capability. As comparisons, nanoscale wicking structures including nanowire [47-50], nanopillar [51-54], nanorod [55], nanotube [56, 57] and nanochannel [58-60] can provide a higher capillary pressure and a lower permeability. Shim et. al [47] found that the aligned nanowires with strengthened capillary wicking has an enhanced wicking coefficient compared to the random nanowires. It was reported that the wicking coefficient on the aligned nanowires increases as the increasing of the height of the aligned nanowires. Poudel [60] et. al investigated the nanochannel's wicking properties and noted the presence of wicking- and evaporation-dominant regimes. Theoretically, the wicking is initially controlled by surface tension and viscous forces with a constant supply of liquid from the droplet in the wicking-dominant regime, while the wicking is controlled by hydrodynamic dissipation in the evaporation-dominant regime.

Moreover, the hierarchical structures composed of the microstructures and nanostructures have also been proposed to enhance the wicking capability. To date, hierarchical structures have been reported including: nanowires with nanocactuses [61], micropillars with nanorods [62], nanopillars with nanowires [63], micropillars with nanopores [64, 65], micromesh with nanostructures [3, 66, 67], nanowires with microgrooves [68]. The hierarchical structures have a greater capacity for wicking because of the increased capillary pressure dictated by the nanostructures and the decreased viscous resistance governed by the microstructures. For instance, Lee et. al [61] proposed a novel hierarchical nanowire arrays which consists of copper nanowires covered with dense copper oxide nanocactuses to enhance the capillary wicking. By this hierarchical structure, more inter-nanowire pore sizes can be provided on the nanocactuses to increase the wicking capabilities. Rokoni et. al [62] the spacing and heights of the hierarchical ZnO nanorods and Si micropillars play a critical role in improving wicking capability. By controlling the spacing and heights of this hierarchical structure, wicking improvement can be adjusted. Wang et. al [63] proposed a three-dimensional hierarchical nanostructures composed of the nanopillars and ZnO nanowires which can increase the surface area, facilitating the liquid flow. Wicking dynamics could be significantly improved due to the existence of the nanowires on the larger pillars, while the viscous resistance could be improved

because the length of nanowires approaches half of adjacent pillar spacing, resulting in the obstruction of the liquid flow. For reducing the viscous resistance produced by the nanoscale structures, Zuruzi et. al [65] demonstrated a new wicking structure employing nanostructured titania grown on titanium micropillars, which can maintain the liquid flow channel for reducing viscous resistance, leading to the improved capillary speed. However, Zheng et. al [64] found that the spreading slow down due to the inhibition of the nanopores with larger depth. For further improving the wicking capability, Alhosani et. al [66] designed a hierarchical micro-meshes with nanostructures which can simultaneously improve the surface wettability and reduce the viscous dissipation to obtain an outstanding wicking performance. Furthermore, the impact of the working fluid, surface shape, and number of layers on the nanostructured micromesh surface were also investigated by Wang et. al [67]. It was discovered that the interlayer microchannels in multilayer plain and fluoridated screens can be used to generate low-resistance flow pathways, enabling the liquid spread. Differing from the above conventional hierarchical structures, Chun et. al [68] proposed the use of hierarchical nanowired surfaces with interconnected V-grooves as liquid transport channels, which can produce superior capillary pressure driven by the nanowires and reduced viscous resistance caused by the interconnected V-grooves.

As a result, the capillary pressure and viscous resistance simultaneously limit the capillary wicking ability of single-scaled structures. As reported, hierarchical designs can greatly improve wicking performance, but greater focus needs to be placed on capillary pressure and viscous resistance that have a large impact on wicking efficiency. In this study, we propose a novel Cu compound hierarchical structures with superior wicking capability, which has been used to significantly enhance the pool boiling heat transfer [69, 70]. However, the enhancement mechanism of this hierarchical structures on capillary wicking has not been revealed. There is no experimental research to investigate the capillary wicking of the Cu compound hierarchical structures. This Cu compound hierarchical structures in this paper are fabricated by the chemical oxidation method, which are easy to be prepared comparing to the conventional hierarchical structures. Differing from the above-mentioned conventional hierarchical structures, in this paper, the microscale structures synthesize from the natural growth of the nanoscale structures. The enhancement mechanism of this hierarchical Cu compound structure on the capillary wicking is discussed in this study, which is valuable in providing a novel fabrication method for manufacturing the hierarchical structures with superior wicking structures and providing a direction of the hierarchical structures' design with outstanding capillary wicking capability.

2. Experimental sections

2.1 Surface fabrication

In this study, cleaning, chemical alteration and vacuum drying are the three primary phases manufacturing of boiling surfaces. The whole copper surfaces

($20mm \times 20mm \times 3mm$) were polished with 2000 grid SiC sandpaper for removing the impurities and remaining the smooth of the surfaces. To move residues, the ultrasonic acetone solution was used to clean the polished copper surfaces for 15 min. Then, the polished surfaces were rinsed with the ultrasonic ethanol and DI water for 10 min, respectively. Finally, these copper surfaces were placed in an oven and heated at 65℃ for 120 min.

Figure 1 shows the surfaces chemical modification process for growing the hierarchical micro/nano structures on the copper surfaces. The experiment materials, sodium hydroxide (NaOH, AR, ≥ 96.0%) and ammonium persulfate ($(NH_4)_2S_2O_8$, AR, 98.0%) were purchased from the Sinopharm Chemical Reagent Co., Ltd. A 100 ml aqueous solution containing 2.5 M NaOH and 0.1 M $(NH_4)_2S_2O_8$ was prepared in a 250 ml glass beaker for generating different micro/nano structures on copper surfaces. The dried and polished copper surfaces were placed into the two solutions at the room temperature for 3 min, 30 min, 60 min and 120 min, respectively. The reaction conditions are summarized in **Table 1**. Besides using the reaction time of 3 min, 30 min, 60 min and 120 min, the same hierarchical structures can also be formed using the reaction time of 15 min, 20 min and 90 min, respectively. In addition, different structures can be synthesized through changing the reactant concentration (1.25 M NaOH and 0.05 M $(NH_4)_2S_2O_8$). Under the circumstance, comparing with the structures synthesized by the reactant concentrations (2.5 M NaOH and 0.1 M $(NH_4)_2S_2O_8$), four types of the same typical hierarchical structures can be formed. A few minutes later, the initial colorless solution in the glass beaker became increasingly blue. In 3, 30, 60 and 120 minutes, the film on the Cu substrate changed from the light-blue colour to the black colour. After the chemical modification in the beaker, the fabricated copper surfaces were rinsed with DI water and placed into the vacuum oven for heating at 60 ℃ to remove the residual solution. After the chemical modification and vacuum drying, blue or dark blue colour appeared on the copper surface.

Table 1. Reaction conditions and results for the oxidation of a copper substrate

Sample no.	Molar ration of NaOH to $(NH_4)_2S_2O_8$ (M)	Concentration of NaOH (M)	Reaction time (min)
1	25:1	2.5	3
2			30
3			60
4			120

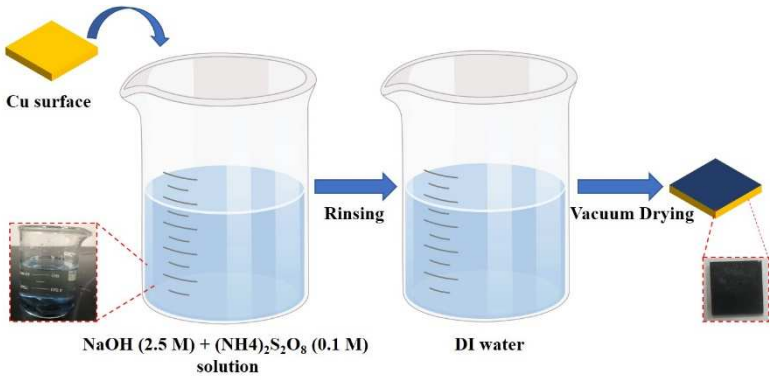

Figure 1. Chemical modification process of copper surfaces.

2.2 Droplet spreading test system

Figure 2a shows the schematic diagram of the droplet spreading experiment. The droplet spreading test system consists of a micro syringe pump, a lifting platform, a light source and a high-speed camera system. In the experiment, 1 μl DI-water droplets obtained from the micro syringe pump were released on the surfaces of samples. To observe the wicking phenomenon, a high-speed camera (Phantom, VEO 410) was set to record 1 s at 1000 fps for capturing the droplet spreading process. High-speed photos were used to examine and capture liquid propagation as the droplet hit the surface. Here, it should be noted that the microsyringe was positioned 3 mm away from the boiling surface in order to minimize mistakes brought on by the effects of gravity and inertia when dropping droplets onto the boiling surfaces. **Figure 2b** shows the droplet spreading and wicking on the Cu hierarchical surfaces. The droplet spreads over the Cu surfaces when the liquid is imbibed into the micro/nanostructured layers and wicked into the space formed by the interlaced micro/nanostructures. A dynamic wicking liquid front spreads forward ahead of the contact line due to the capillary wicking effect. **Figure 2c** shows the captured image of droplet spreading and wicking. $\boldsymbol{R_f}$ represents the capillary wicking radius (from center to dynamic wicking liquid front) and $\boldsymbol{R_c}$ represents the droplet spreading radius (from center to contact line). The wicking distance l is the distance between $\boldsymbol{R_f}$ and $\boldsymbol{R_c}$. Through analyzing the high-speed images used with Image J software, the wicking distance with time was measured. To evaluate the wicking capability of micro/nanostructures, the Washburn approach which balances the capillary pressure and the viscous resistance is widely utilized, where the wicking distance is proportional to $t^{1/2}$. Therefore, the model to predict the wicking distance as a function of time can be obtained as follows [35, 36, 47]:

$$l = \sqrt{\frac{2P_{cap}}{K}t} = W\sqrt{t} \quad (1)$$

where P_{cap} is the capillary pressure, K is the permeability, which are affected by the surface morphology. However, the permeability K and capillary pressure P_{cap} are difficult to be directly measured for the hierarchical surface structures. $W = (2P_{cap}/K)^{1/2}$ is the wicking coefficient, which represents the wicking capability [35].

According to Eq. (1), we can predict that the high wicking coefficient can be obtained from the high capillary pressure corresponding to the low viscous resistance.

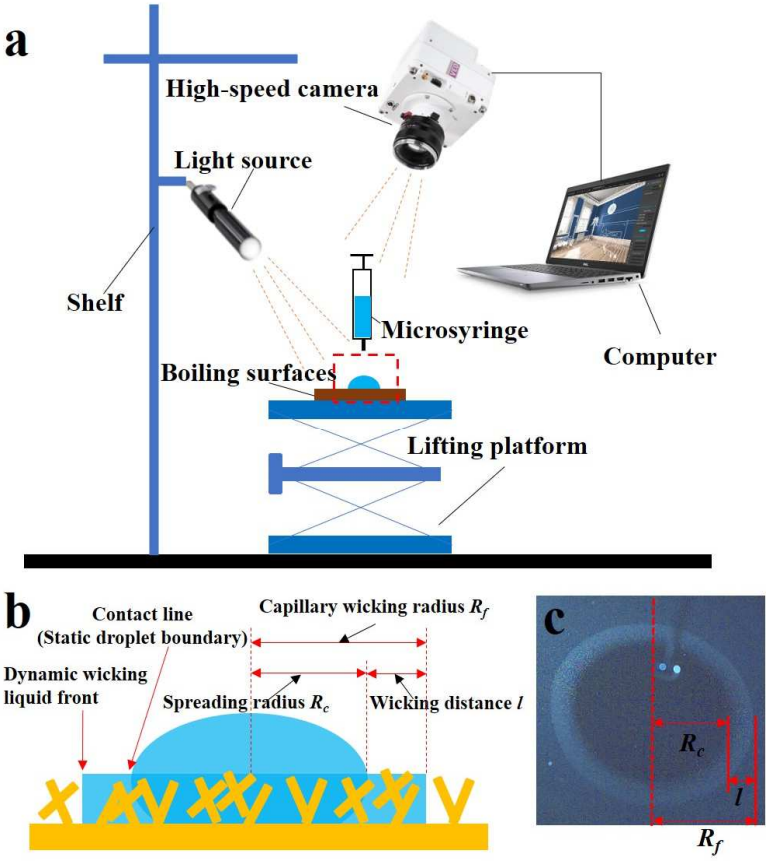

Figure 2. (a) Droplet spreading experimental setup (b) Schematic of droplet spreading and wicking (c) Captured image of droplet spreading and wicking

2.3 Water absorption test system

As illustrated in **Figure 3**, a capillary tube with an inner diameter ($\boldsymbol{R_t}$) of 1 mm filled with water of 2 ± 0.2 μL from the bottom was placed above the surface. When contacting with the surface, the height of water in the capillary tube can reduce due to the absorption of the micro/nanostructures on the surface. By using high-speed camera, the change of liquid level Δh and the wicking process can be recorded and calculated. The initial height of water is H_{init} and thereby the initial volume of water is

$$V_{initial} = \pi R_t^2 H_{initial} \tag{2}$$

while the volume of water with the time is

$$V = \pi R_t^2 H \tag{3}$$

Therefore, the absorbed volume of water is

$$V = \pi R_t^2 H_{initial} - \pi R_t^2 H \quad (4)$$

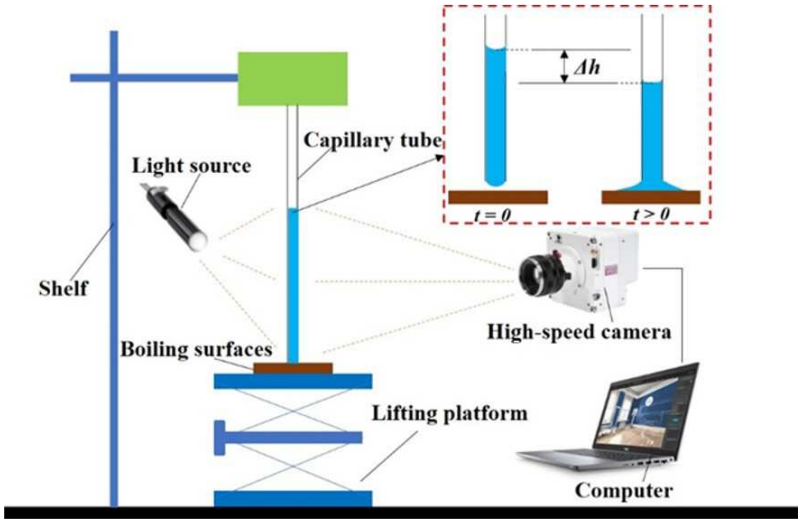

Figure 3. Water absorption experiment

2.4 Morphology characterization methods

Scanning electron microscopy (SEM, Sirion 200, FEI, America) and atomic force microscopy (AFM, Dimension Edge, Bruker) techniques were used to clearly identify the surface morphology properties the surface roughness of the Cu hierarchical micro/nanocrystals. The contact angle was measured by a contact angle meter (DSA 25S, KRUSS, German) under atmosphere pressure. A 2 μL droplet DI water was dropped on the Cu surfaces, and the contact angles can be measured.

3. Results and discussions

3.1 Surfaces morphology characteristics

Figure 4 shows the SEM images of Cu substrate, NG, NGMP, NGMF and NSMF. As shown in **Figure 4a**, after polishing process, the flat surface can be observed on the Cu substrate. As shown in **Figure 4b**, after the Cu substrate immersing into the solutions for 3 min, the interesting nanograss forests (NG) can be observed on the Cu substrate. During the growth process of the nanograss on the substrate, nanograss tips can be intertwined with each other, resulting in the formation of the micro-petals. And the nanograss and micro-petals (NGMP) coexist on the substrate almost half and half, as illustrated in **Figure 4c**. Thereby, increasing the immersion time to 30 min, the micro-petal shaped structures can be formed on the nanograss, as depicted in **Figure 4c**. With this immersion time, the size of the nanograss is almost unchanged, and the micro-petals grow bigger with a dimeter of 2 ~ 4 μm and covers the Cu substrate more uniformly with the nanograss forests under them. Further increasing the immersion time to 60 min, the micro-petals on the nanograss synthesized to the micro-flowers (NGMF), covering the Cu substrate, as shown in **Figure 4d**. Compared with the above hierarchical NGMP, the NGMF has denser nanograss lying under the

synthesized micro-flowers with dimeter of about 4 μm, as shown in **Figure 4d**. Furthermore, the magnified SEM image of a micro-flower illustrates that the thickness of the flower petals is approximately 50 nm (**Figure 4d**). In comparison with the magnified SEM images of the nanongrass in **Figure 4b**, **c** and **d**, more nanograss tips can be synthesized to the micro-flowers and nanograss are stacked firmly on the substrate, as depicted in **Figure 4d**. The nanograss forests grow on the Cu substrate, exhibiting a large amount of the slit-like holes under the micro-petals and micro-flowers, as seen in **Figure 4b** and **c**. Further increasing immersion time to 120 min, the SEM image of this hierarchical structure is composed of small nanosheets and micro-flowers (NSMF), as shown in **Figure 4e**. With sufficient reaction time, the thick sheets were formed by the nanoneedles under the micro-flowers.

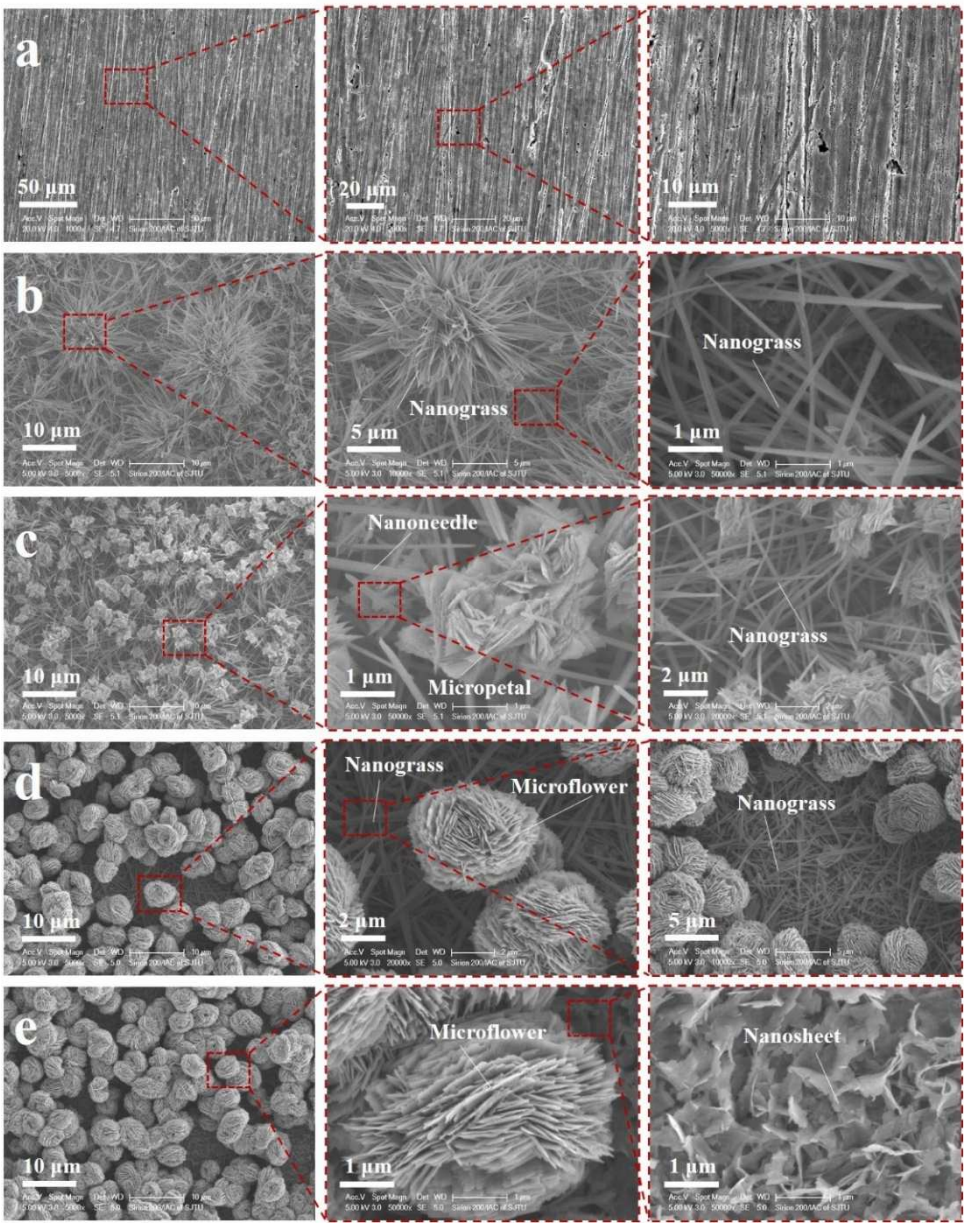

Figure 4. SEM images of (a) Cu (b) NG (c) NGMP (d) NGMF (e) NSMF.

X-ray diffraction (XRD) analysis is used to determine the structure and phase of the samples. The XRD patterns of Cu substrate can be recorded on the various samples, which can imply that the substrate contains solely a cubic Cu phase with lattice reasonable parameters of a = b = c = 3.615 Å (JCPDS card 04-0836), as shown in **Figure 5a**, **b**, **c**, **d** and **e**. The diffraction peaks of $Cu(OH)_2$ from the Cu substrate can be indexed, as shown in **Figure 5b**. The derived parameters, a = 2.949 Å, b = 10.590 Å, c = 5.256 Å, are consistent with the values in the literature: a = 2.947 Å, b = 10.5930 Å, c = 5.2564 Å. **Figure 5c** exhibits the observed diffraction peaks of $Cu(OH)_2$ and CuO with standard parameter. Also, **Figure 5d** illustrates that the observed diffraction peaks can be indexed to monoclinic CuO (JCPDS card 48-1548). As shown in **Figure 5e**, the diffraction peaks of XRD pattern are consistent with those of monoclinic CuO (JCPDS card 48-1548). Therefore, the main component of NG and NGMP is $Cu(OH)_2$ and CuO, respectively. Also, the main component of NGMF and NSMF is CuO with abundant reaction time.

Figure 6 shows the AFM images which can exhibit the surface topography and roughness of Cu, NG, NGMP, NGMF and NSMF structures. Due to the polishing process, the untreated Cu surface exhibits a flat surface. Also, the chemical modification causes surfaces to gradually generate and increase rough nanoscale features. The surface roughness of the Cu, NG, NGMP, NGMF and NSMF is 1.07 μm,60.52 nm, 329.45 nm, 353,56 nm and 388.84 nm, respectively.

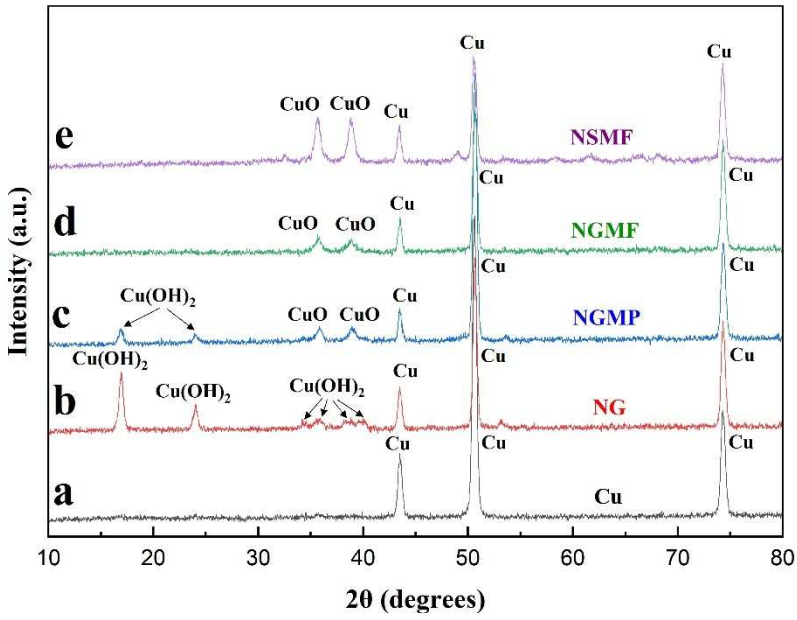

Figure 5. XRD images of the samples (a) Cu (b) NG (c) NGMP (d) NGMF (e) NSMF

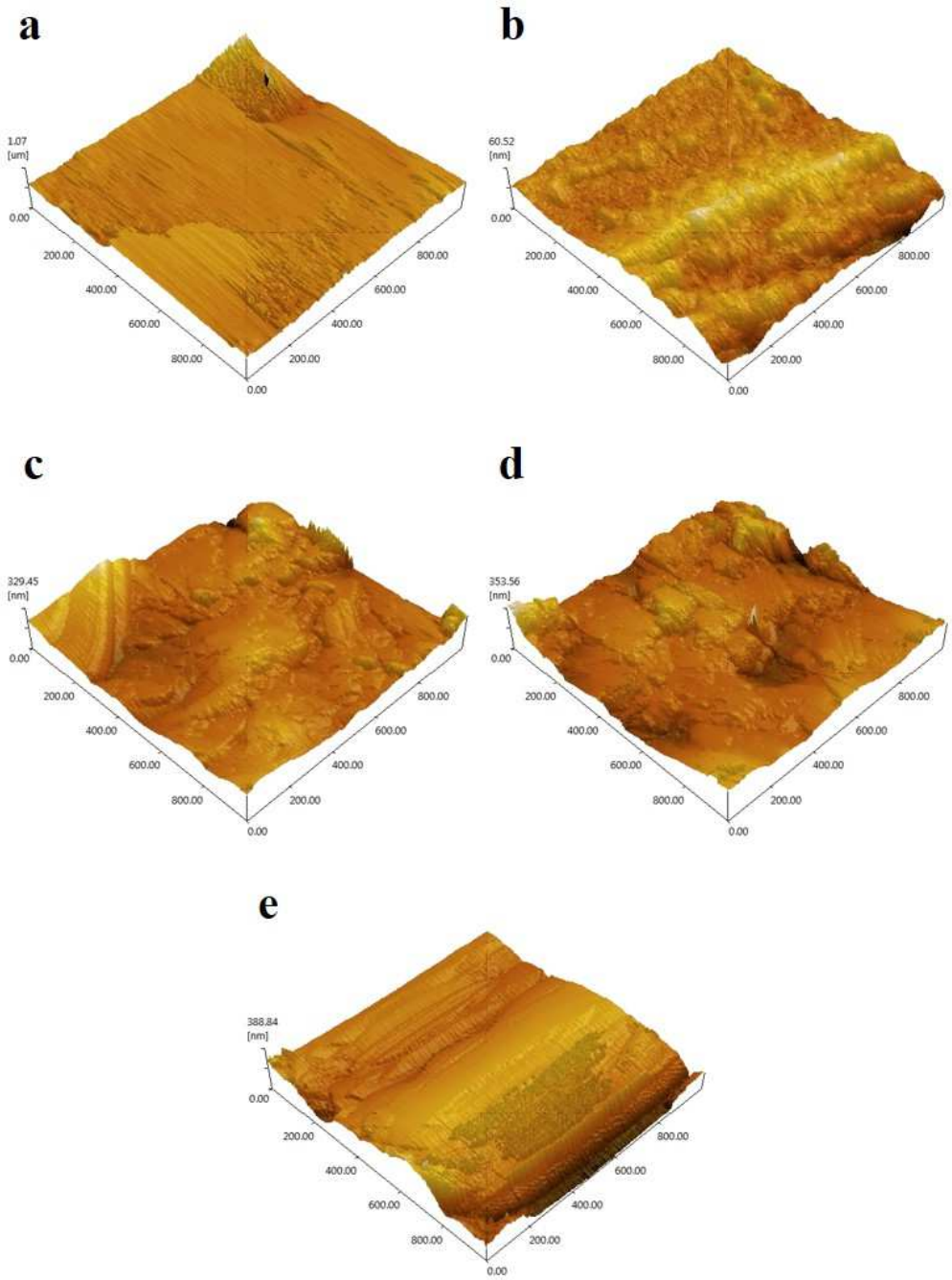

Figure 6. AFM images of (a) Cu (b) NG (c) NGMP (d) NGMF (e) NSMF

3.2 Wetting property of various Cu compound surfaces

As shown in **Figure 7a**, the untreated Cu surface exhibits the hydrophilicity with the contact angle of 47°, and the contact angle has no significant change with time. However, the wettability on Cu hierarchical surfaces including NG, NGMP, NGMF and NSMF has been enhanced with contact angle ≈ 0°, as shown in **Figure 7b**, **c**, **d** and **e**. As a result, following treatment, the contact angles of the four samples reduced. With respect to the NG, NGMP, NGMF and NSMF surfaces, when the droplets touch the surface, the droplets can be absorbed into the micro/nanostructures on the Cu

substrate. Finally, the droplets can be absorbed completely, resulting in the contact angle of 0°. Moreover, due to the diversity of surface morphology and properties, different dynamic evolution time of contact angle can be observed on the NG, NGMP, NGMF and NSMF surfaces.

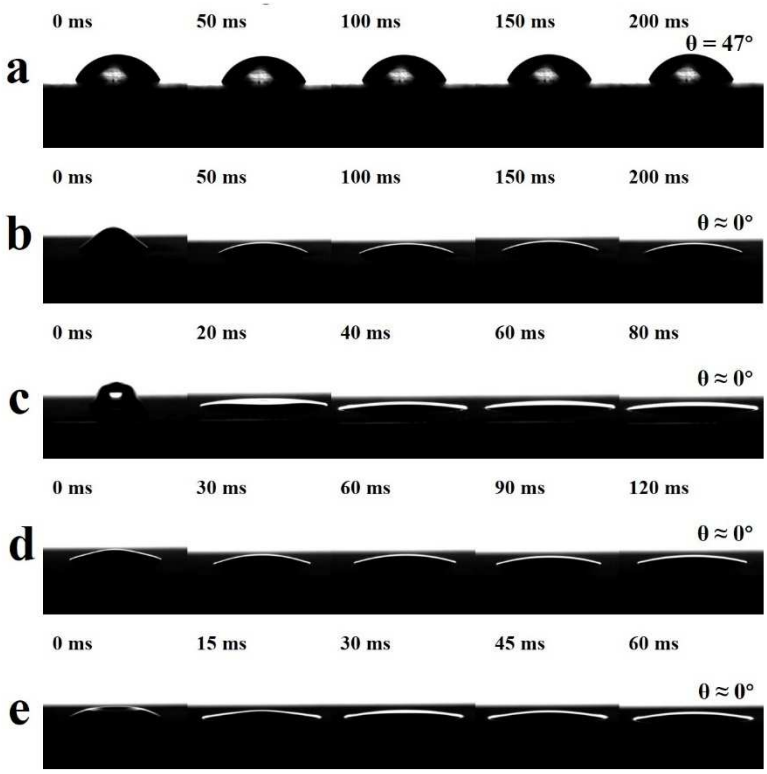

Figure 7. Dynamic evolution of contact angle on (a) Cu (b) NG (c) NGMP (d) NGMF (e) NSMF.

3.3 Capillary spreading of Cu hierarchical structures

Figure 8 shows the high-speed camera images of dynamic wicking on the Cu, NG, NGMP, NGMF and NSMF surfaces. As shown in **Figure 8**, with respect to the NG, NGMP, NGMF and NSMF surfaces, according to the motion of the dynamic wicking liquid front and static droplet boundary, synchronous spreading stage and capillary spreading stage can be observed. At the initial synchronous spreading stage, the dynamic wicking liquid front and contact line can forward together, while the dynamic wicking liquid front can move ahead of the contact line at the capillary spreading stage. This indicates that water droplets can be quickly absorbed by the micro/nanostructures on the NG, NGMP, NGMF and NSMF surfaces. Nevertheless, with respect to the Cu surface, no significant separation between the dynamic wicking liquid front and contact line can be observed. This is attributed to the fact that no absorbed micro/nanostructures can drive the liquid suction on the Cu substrate.

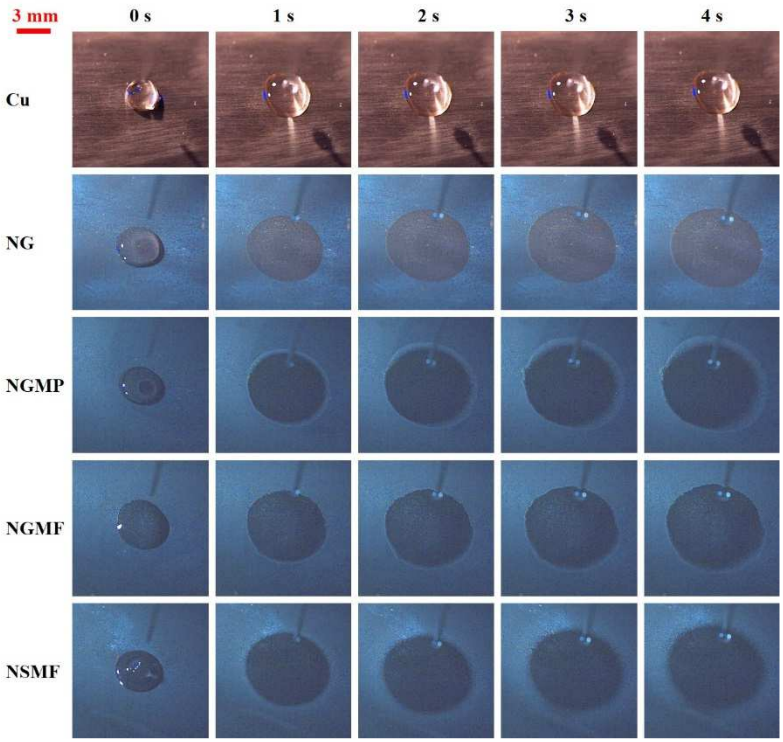

Figure 8. High-speed camera images of dynamic wicking on various samples.

Figure 9 shows the dynamic droplet radii R_f on the NG, NGMP, NGMF and NSMF surfaces. When touching the surfaces, due to the large capillary pressure at the initial synchronous spreading stage, the liquid can spread rapidly through the wicking structures. The transient liquid wicking front rise rates (dR_f/dt) of all the four Cu hierarchical structures decreases as a function of the increase of the wicking front radius. This is attributed to the fact that the viscous resistance will increase while the capillary pressure maintains unchanged when expanding the dynamic liquid wicking front at the initial stage. The images show an apparent tendency that each sample has a large wicking radius during the extremely short time period. At any given time during the first stage, the wicking radius of NSMF is greater than that of the other structures. For example, the wicking radius on NSMF at t = 0.05 s is 3.544 mm, 40.7 %, 13.3 % and 28.5 % larger than that on NG, NGMP, NGMF, respectively. The hierarchical Cu compound structures including NGMP, NGMF and NSMF exhibits a higher wicking speed than single nanoneedle forests. After 0.5 s, due to the improved viscous resistance, the wicking distance rate decreased as the increase of spreading time.

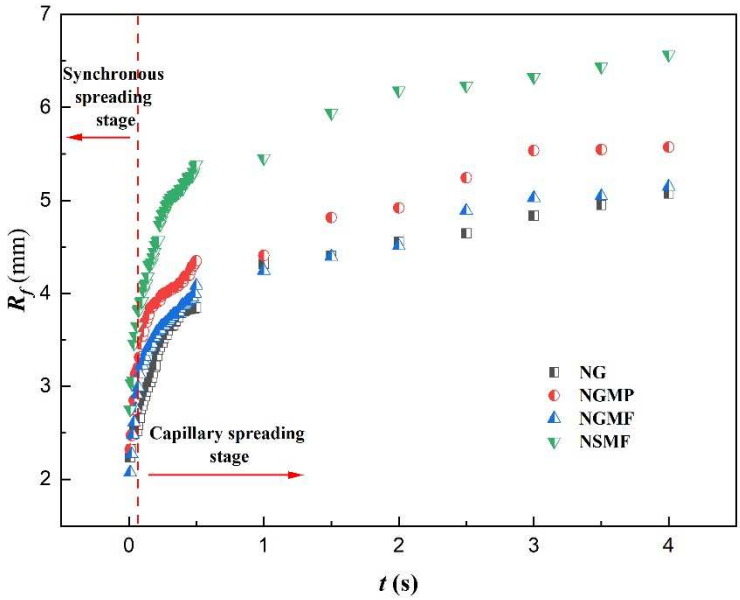

Figure 9. Dynamic liquid wicking front R_f

Figure 10a, **b**, **c** and **d** illustrate the variation of the liquid wicking front radius R_f and contact line radius R_c. Two stages can be observed in the droplet spreading process: synchronous spreading and capillary spreading. In synchronous spreading stage, the R_f and R_c spread together. In capillary spreading stage, the dynamic wicking liquid front advance well ahead of the contact line because the dynamic wicking liquid front further increase while the contact line remains unchanged. For the NG, NGMP and NGMF structures, the dynamic wicking liquid front begins to spread ahead of the contact line after the time reaches 0.05 s according to the occurrence of different slopes of R_f and R_c with the log-log plots. It is obvious that the R_f follows the power-law behavior $R_f \propto t^n$ during the capillary spreading process. As illustrated, the NSMF can enter into the capillary spreading stage earlier than the other surfaces, indicating that the NSMF has the strongest capillary spreading velocity. In special, the exponent values n_f of the power-law fittings of R_f on the Cu hierarchical surfaces are 0.216, 0.122, 0.136 and 0.184, respectively.

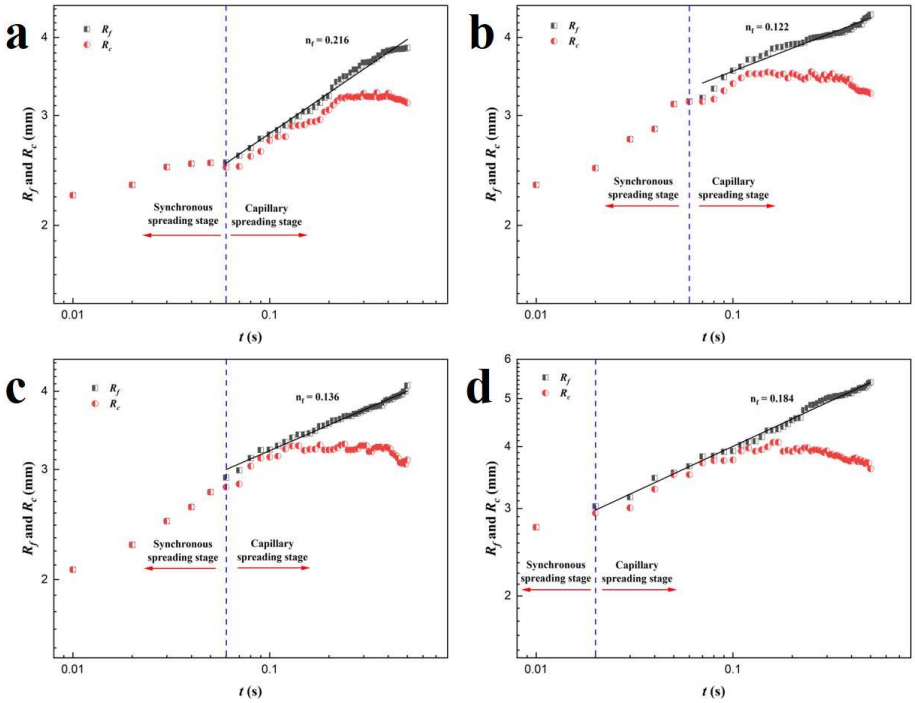

Figure 10. Variation of the liquid wicking front radius R_f and contact line radius R_c on the (a) NG (b) NGMP (c) NGMF (d) NSMF

Figure 11 shows the wicking coefficient as a function of the square root of time on the whole Cu hierarchical structures in the initial 0.5 s. A good liner fit between the wicking distance and square root of time can be observed, which has been expressed by the Equation (1). In obvious, comparing with the NG, NGMP and NGMF structures, the NSMF exhibits the largest wicking coefficient of 3.77 mm/s$^{0.5}$. The wicking coefficient of the NG, NGMP and NGMF is 1.53, 1.73 and 2.13 mm/s$^{0.5}$, respectively. In addition, the hierarchical structures including NGMP, NGMF and NSMF has the larger wicking coefficient than the single-scaled NG structure. A possible explanation is the single-scaled pores or spacings provided by the NG structure can decrease the ratio of capillary pressure and viscous resistance. While the hierarchical structures can provide the strengthened capillary pressure driven by the nanostructures and the reduced viscous resistance driven by the microstructures, resulting in the enhancement in wicking coefficient on the hierarchical structures NGMP, NGMF and NSMF.

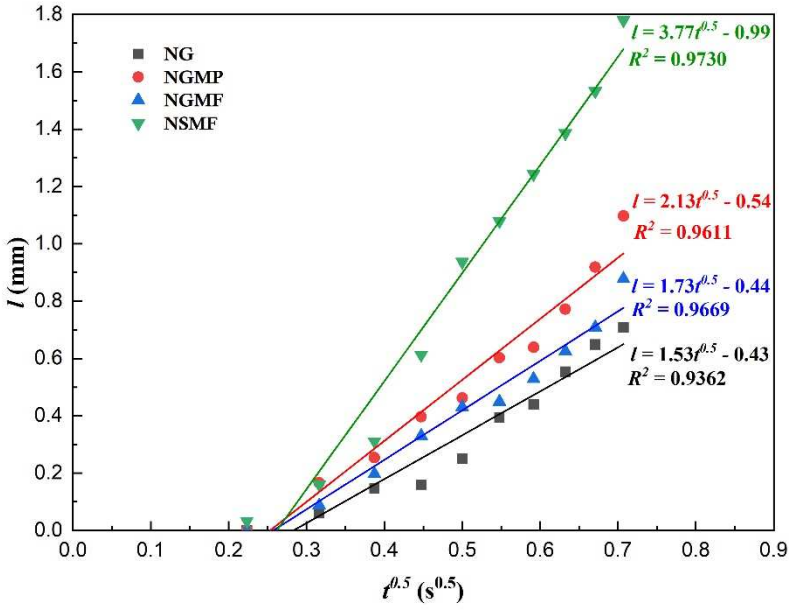

Figure 11. Wicking coefficient of NG, NGMP, NGMF and NSMF

3.4 Mechanism of the enhanced wicking on Cu hierarchical structures

The capillary force on the micro/nanostructures and the frictional force of the water can both control how much water is transported within them. The capillary force and frictional force can be expressed as below:

$$F_{cap} = C_1 R_{geometry} \sigma \cos\theta A_{area} = C_2 \Delta P_{cap} A_{area} \quad (5)$$

$$F_{friction} = B_1 \mu U R_f = B_1 \mu R_f \frac{dR_f}{dt} \quad (6)$$

where ΔP_{cap} is the capillary pressure, σ is the surface tension of the liquid, $R_{geometry}$ is the geometry curvature of the liquid, θ is the contact angle, A_{area} is the cross-sectional area, R_f is the dynamic wicking liquid front, μ is the viscosity, C_1, C_2 and B_1 is the empirical constants. **Figure 12a** shows the schematic diagram of water spreading related with the capillary force and frictional force on the surface, which can display the Equation (5) and (6). The capillary pressure between the spacing of the micro/nanostructures can govern the capillary force (ΔP_{cap}), which can be calculated as follows:

$$F_{cap} = \Delta P_{cap} \times A_{area} = \Delta P_{cap} P \delta\varepsilon = \Delta P_{cap} 2\pi R_f \delta\varepsilon \quad (7)$$

where P is the perimeter of the dynamic wicking liquid front, δ is the thickness of micro/nanostructures, ε is the porosity of micro/nanostructures. At the initial stage, the capillary force is the dominate force, much larger than the frictional force, which can drive the contact line and dynamic wicking liquid front forward together with great speed, forming the synchronous spreading. When the synchronous spreading stage transforms to the capillary spreading stage, the capillary force and frictional

force are balanced ($F_{cap} = F_{friction}$). According to the **Figure 9c**, **d**, **e** and **f**, the $\boldsymbol{R_f}$ and t are in good agreement with the expression of $\boldsymbol{R_f} \propto t^n$. As the spreading time increases, the frictional force is larger than the capillary force ($F_{cap} < F_{friction}$), and the dynamic wicking liquid front continues to spread with decreased velocity. Ultimately, due to the limited volume of water droplet, the liquid spreading will disappear.

As shown in **Figure 12b** and **f**, on the single-scaled NG surface, due to the dense nanograss with narrow spacing or small pores for water transport, the friction (viscous resistance) is enlarged. As comparisons, during the growth process, the tips of the nanograss can be sticked together, forming the micro-petals and micro-flowers on the tips, as well as grooves on the bottom, as shown in **Figure 12c**, **d, g** and **h**. With this groove structure, friction can be reduced, water transport through the channel in terms of the grooves with about 5 ~ 10 μm diameter. In addition, the NSMF has the micropores which are stacked by the micro-flowers illustrated in **Figure 12e** and **i**, resulting in the rapid water transporting in the initial stage. Therefore, when the water droplet first contacts the NGMP, NGMF and NSMF surfaces, the vertical capillary wicking will absorb the water vertically, while the channel composed of the microstructures with large dimensions can provide the flow path with low resistance for water transporting. Therefore, more absorbed volume and faster absorbed velocity of water can be observed at the initial stage.

Further increasing the spreading time, as above-mentioned, the frictional force is larger than the capillary force, leading to the decreased absorbed velocity of water. Differing from the NGMP, NGMF and NSMF surfaces, the NG surface has the single-scaled spacing between the nanograss for producing the stable capillary force and frictional force, which can drive the water droplet forward and water absorbing at a stable speed. On the contrast, when the water droplet spreading enters the capillary spreading stage, the horizontal capillary force plays a role as the dominate force for driving the water froward, resulting in the dynamic wicking liquid front advancing ahead of the contact line. As shown in **Figure 12d** and **h**, the nanongrass on the Cu substrate intertwines with each other, which may make the obstruction of the water transport at the horizontal, resulting in the smaller $\boldsymbol{R_f}$ due to the limited capillary force and strengthened frictional force comparing with the NGMP and NSMF surfaces. With regarding to the NGMP surface, the spacings between the adjacent nanongrass provide the capillary force for water transporting, while the grooves can serve as the flow channel for water transporting with low frictional force, as shown in **Figure 12c** and **g**. This means that the NGMP can drive the water spreading with a larger distance compared with the NGMF due to the low frictional force. As comparisons, the NSMF also can provide the flow channel for water transport, while the microchannels resulting from the stacked micro-flowers is large than the grooves (**Figure 12e** and **i**). Thereby smaller frictional force can be produced at the horizontal direction during the water spreading process compared with the NGMP. Meanwhile, the interlaced nanosheets on the bottom can produce strengthened capillary force due to the smaller spacing distance between the adjacent nanosheets, which can produce the stronger capillary pressure for driving the water transport. Herein, the NSMF can drive the water droplet with a largest distance because of the higher capillary force and lower

frictional force.

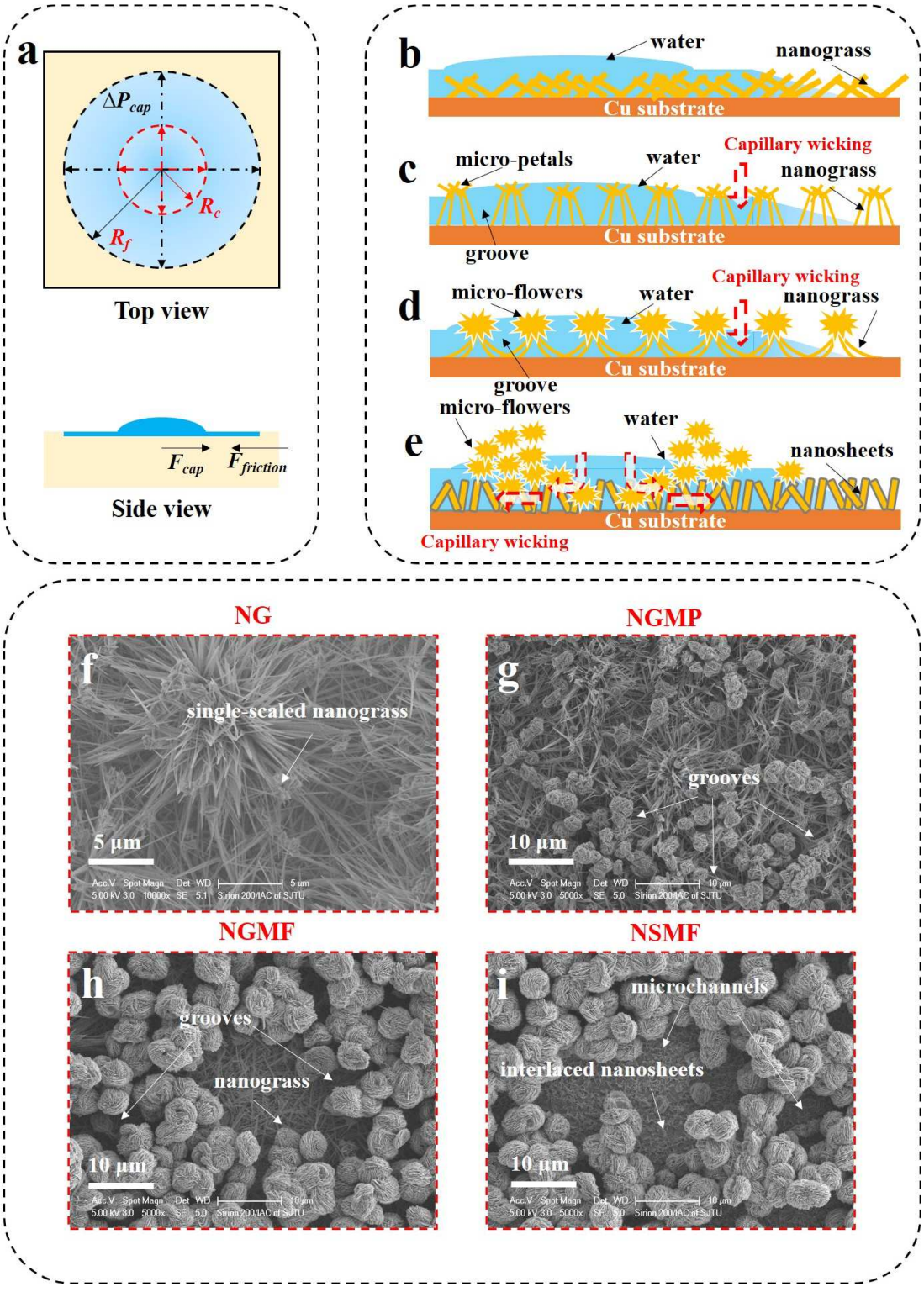

Figure 12. (a) Schematic diagram of capillary force and frictional force related with the water spreading; Illustration of water spreading on (b) NG (c) NGMP (d) NGMF (e) NSMF; SEM images of (f) NG (g) NGMP (h) NGMF (i) NSMF

Overall, smaller spacing can produce the larger capillary pressure and viscous resistance, while the larger spacing can produce the smaller capillary pressure and

viscous resistance [50]. The NG and NGMF with single-scaled spacing has the worse water penetration, while the NGMF and NSMF with multi-scaled spacing has the better penetration. As shown in **Figure 12e**, we achieve an improved hierarchical structure (NSMF) for enhancing capillary wicking capability. The rapid synchronous spreading results from the micropores between micro-flower clusters with reduced frictional force. While the capillary pressure provided by the nanosheets on the Cu substrate can drive the water forward. Through the micro-channel with reduced frictional force produced by micro-flowers, the water can be driven much farther than the other hierarchical surfaces. In general, combination of the micropores between micro-flower clusters for synchronous spreading, nanosheets for providing capillary pressure and micro channels for wicking liquid to flow, the NSMF can increase wicking coefficient, resulting in lowers viscous resistance and encourages capillary wicking.

3.5 Water absorption of Cu hierarchical structures

Figure 13 shows the water absorption on the Cu, NG, NGMP, NGMF and NSMF surfaces as time increases. In obvious, the height of water in the capillary tube remains unchanged on the Cu substrate, indicating that Cu substrate cannot absorb the water. Furthermore, the height of the water inside of the other capillary tubes is decreasing, exhibiting the NG, NGMP, NGMF and NSMF surfaces absorb the water well. Furthermore, the capillary tube of the NSMF has the lowest height of the water among the whole samples, which indicates the best water absorption performance.

Figure 14 shows the absorbed volume of water and height of water in the capillary tube as a function of time. The NSMF exhibits the largest absorbed volume of water with 0.294 μL at 0.5 s, which is 68 %, 26.2 % and 44.8 % higher than the NG, NGMP and NGMF, respectively. As illustrated, the NG has the lower absorbed volume velocity than the other hierarchical structures in the initial 0.1 s. Liquid spreads on the NG, only attributed to the nanograss, while hierarchical structures NGMP, NGMF and NSMF has the larger spacing or pores for liquid flow at the initial stage, leading to the faster absorbed volume velocity. Furthermore, the hierarchical structures NGMP, NGMF and NSMF has the different absorbed volume velocity when the spreading time reaches 0.2 s, which may be caused by the friction existed in the structures, by which the absorbed volume velocity decreases.

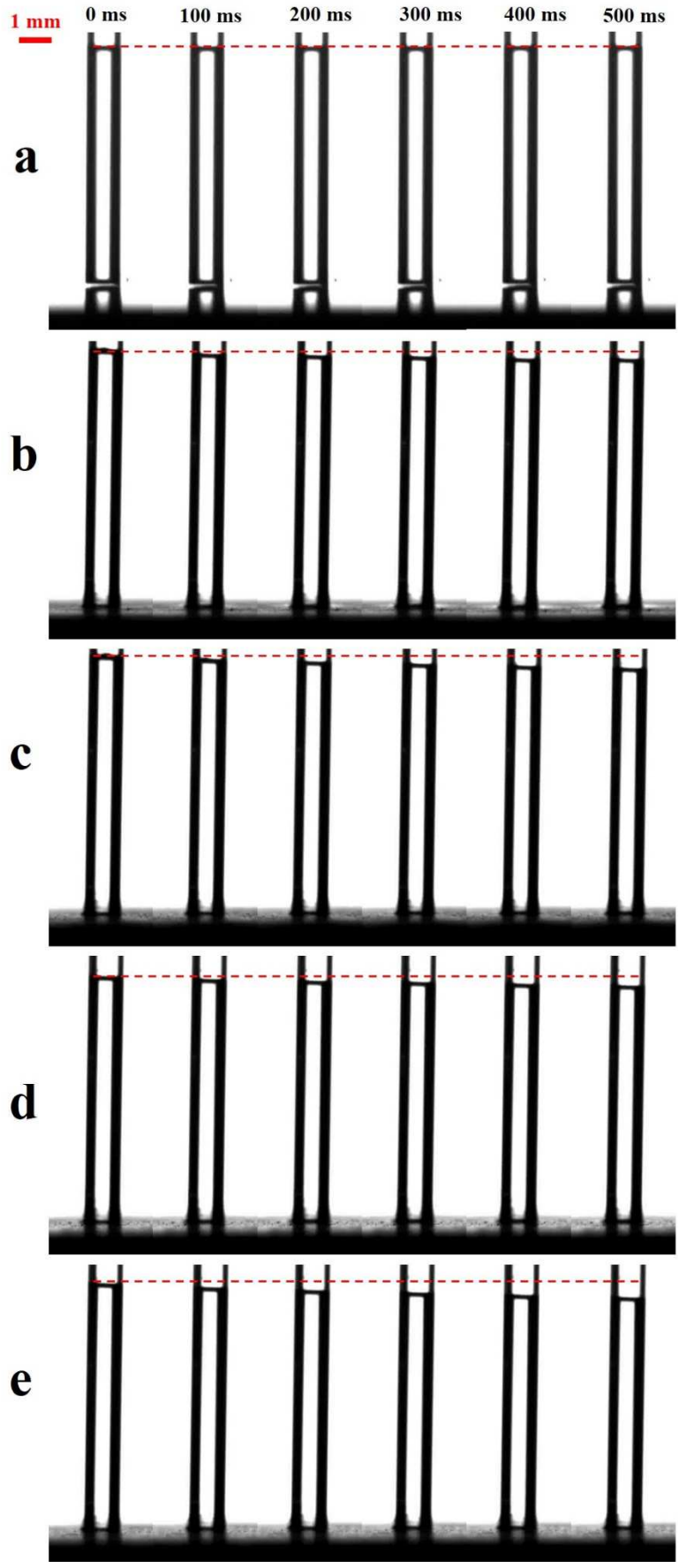

469

470 **Figure 13**. Water absorption on (a) Cu (b) NG (c) NGMP (d) NGMF (e) NSMF

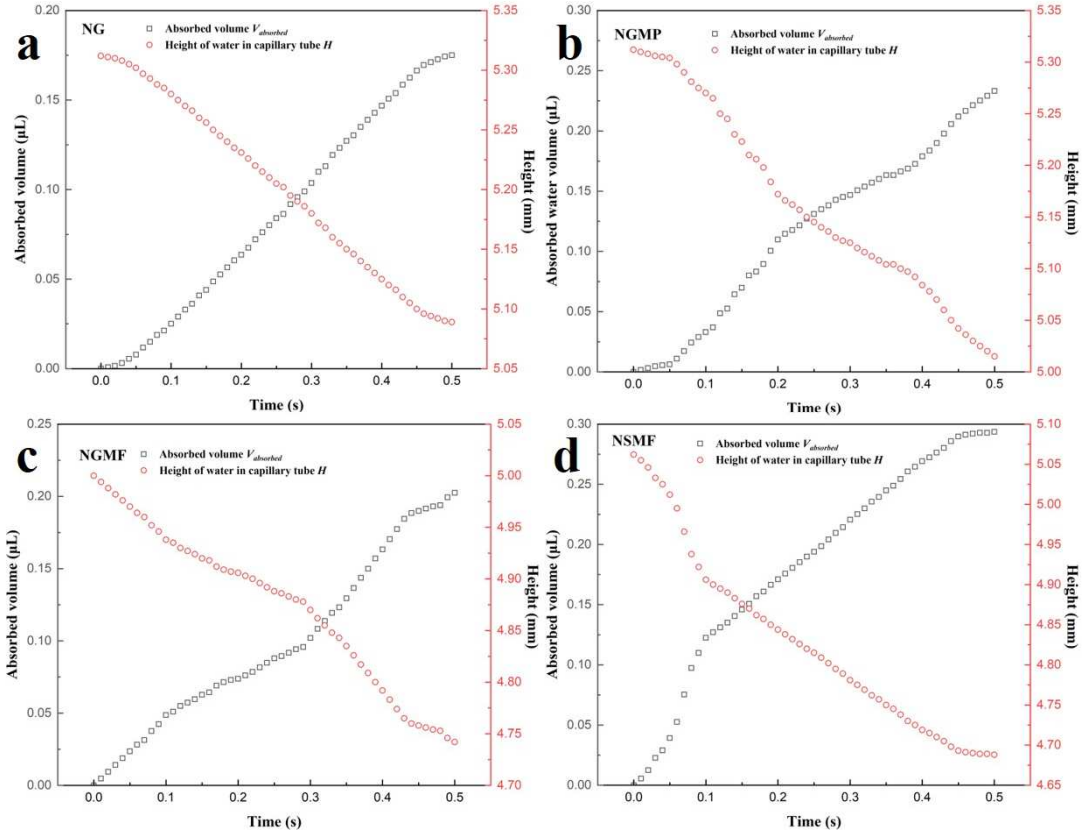

Figure 14. Absorbed volume of water and height of water in capillary tube (a) NG (b) NGMP (c) NGMF (d) NSMF

4. Conclusions

In this paper, four Cu compound structures are fabricated and the effect of surface morphology on capillary wicking capability is investigated. The main conclusions have been drawn based on experiments:

(1) In-situ micro/nanocrystal structures on Cu substrates with prominently improved wicking capacity is fabricated by the chemical oxidation method. The NG structure has the single-scale pores for enhancing the capillary wicking. The NGMP, NGMF and NSMF possess the nanograss layer or nanosheet layer lying on the intrinsic Cu substrate, and the micro-petal or micro-flower layer on the top, resulting in the enhanced capillary wicking.

(2) The wettability experiments show that the oxidation treatment can significantly increase the surface hydrophilicity. In addition, different surface morphology and roughness result in different surface wettability, and hemi-wicking phenomenon can occur on the NG, NGMP, NGMF and NSMF because the critical contact angle is larger than the apparent contact angle.

(3) The results of the droplet spreading experiments indicate that the wicking capability of the hierarchical structures is superior to wicks consisting of single-

scale nanograss. The rapid capillary wicking coefficient of 3.77 mm/s$^{0.5}$ on the NSMF hierarchical layers can be obtained. This is attributed to the combination of fine pores and large liquid channels that enables an excellent comprehensive wicking capability on the in-situ hierarchical wicks.

(4) A possible mechanism has been proposed to explain the role of surface morphology for enhancing water transport. The inter-micro petal or inter-micro flower pores can serve as the major pathway water circulation on the nanograss or nanosheet layers. Meanwhile, the viscos resistance is significantly affected by the surface chemistry and the pore size of the materials.

Acknowledgements

This research is financially supported by National Key Research and Development Program (No.2022YFE0198800), and National Natural Science Foundation of China (No. 52076139).

Reference

[1] R. Wen, X. Ma, Y.-C. Lee, R. Yang, Liquid-Vapor Phase-Change Heat Transfer on Functionalized Nanowired Surfaces and Beyond, Joule, 2(11) (2018) 2307-2347.

[2] R. Wen, S. Xu, D. Zhao, L. Yang, X. Ma, W. Liu, Y.-C. Lee, R. Yang, Sustaining enhanced condensation on hierarchical mesh-covered surfaces, National Science Review, 5(6) (2018) 878-887.

[3] R. Wen, S. Xu, Y.-C. Lee, R. Yang, Capillary-driven liquid film boiling heat transfer on hybrid mesh wicking structures, Nano Energy, 51 (2018) 373-382.

[4] X. Qiu, H. Yang, M. Dejam, S.P. Tan, H. Adidharma, Experiments on the Capillary Condensation/Evaporation Hysteresis of Pure Fluids and Binary Mixtures in Cylindrical Nanopores, The Journal of Physical Chemistry C, 125(10) (2021) 5802-5815.

[5] X. Li, S. Wang, R. Wen, X. Ma, R. Yang, Liquid film boiling enabled ultra-high conductance and high flux heat spreaders, Cell Reports Physical Science, 3(3) (2022).

[6] R. Gimenez, G. Soler-Illia, C.L.A. Berli, M.G. Bellino, Nanopore-Enhanced Drop Evaporation: When Cooler or More Saline Water Droplets Evaporate Faster, ACS Nano, 14(3) (2020) 2702-2708.

[7] H. Zhang, Z. Guo, Near-junction microfluidic cooling for GaN HEMT with capped diamond heat spreader, International Journal of Heat and Mass Transfer, 186 (2022).

[8] R. Liu, Z. Liu, Self-pumping ultra-thin film evaporation on CNT-embedded silicon nitride nanopore membrane, Nano Research, 15(3) (2021) 1725-1729.

[9] L. Gong, Y.-P. Xu, B. Ding, Z.-H. Zhang, Z.-Q. Huang, Thermal management and structural parameters optimization of MCM-BGA 3D package model, International Journal of Thermal Sciences, 147 (2020).

[10] J. Li, Y. Zhao, J. Ma, W. Fu, X. Yan, K.F. Rabbi, N. Miljkovic, Superior Antidegeneration Hierarchical Nanoengineered Wicking Surfaces for Boiling Enhancement, Advanced Functional Materials, 32(8) (2021).

[11] H. Jarrett, M. Wade, J. Kraai, G.L. Rorrer, A.X. Wang, H. Tan, Self-powered microfluidic pump using evaporation from diatom biosilica thin films, Microfluidics and Nanofluidics, 24(5) (2020).

[12] A. Piovesan, T. Van De Looverbosch, P. Verboven, C. Achille, C. Parra Cabrera, E. Boller, Y. Cheng, R. Ameloot, B. Nicolai, 4D synchrotron microtomography and pore-network modelling for direct in situ capillary flow visualization in 3D printed microfluidic channels, Lab Chip, 20(13) (2020) 2403-2411.
[13] B. Ma, J. Chi, C. Xu, Y. Ni, C. Zhao, H. Liu, Wearable capillary microfluidics for continuous perspiration sensing, Talanta, 212 (2020) 120786.
[14] C. Achille, C. Parra-Cabrera, R. Dochy, H. Ordutowski, A. Piovesan, P. Piron, L. Van Looy, S. Kushwaha, D. Reynaerts, P. Verboven, B. Nicolai, J. Lammertyn, D. Spasic, R. Ameloot, 3D Printing of Monolithic Capillarity-Driven Microfluidic Devices for Diagnostics, Adv Mater, 33(25) (2021) e2008712.
[15] M.S. Khan, D. Kannangara, G. Garnier, W. Shen, Effect of liquid droplet impact velocity on liquid wicking kinetics in surface V-grooves, Chemical Engineering Science, 66(23) (2011) 6120-6127.
[16] W. Li, Y. Joshi, Capillary-Assisted Evaporation/Boiling in PDMS Microchannel Integrated with Wicking Microstructures, Langmuir, 36(41) (2020) 12143-12149.
[17] Y. Ye, Y. Zhao, J. Cheng, M. Li, C. Huang, Design, fabrication and characterisation of Si-based capillary-driven microfluidic devices, Micro & Nano Letters, 13(12) (2018) 1682-1687.
[18] J. Xu, T. Li, J. Chao, S. Wu, T. Yan, W. Li, B. Cao, R. Wang, Efficient Solar-Driven Water Harvesting from Arid Air with Metal-Organic Frameworks Modified by Hygroscopic Salt, Angew Chem Int Ed Engl, 59(13) (2020) 5202-5210.
[19] X. Gou, Z. Guo, Hybrid Hydrophilic-Hydrophobic CuO@TiO2-Coated Copper Mesh for Efficient Water Harvesting, Langmuir, 36(1) (2020) 64-73.
[20] Y. Hu, Z. Fang, X. Wan, X. Ma, S. Wang, S. Fan, M. Dong, Z. Ye, X. Peng, Carbon nanotubes decorated hollow metal–organic frameworks for efficient solar-driven atmospheric water harvesting, Chemical Engineering Journal, 430 (2022).
[21] H.G. Andrews, E.A. Eccles, W.C. Schofield, J.P. Badyal, Three-dimensional hierarchical structures for fog harvesting, Langmuir, 27(7) (2011) 3798-3802.
[22] C. Li, Y. Liu, C. Gao, X. Li, Y. Xing, Y. Zheng, Fog Harvesting of a Bioinspired Nanocone-Decorated 3D Fiber Network, ACS Appl Mater Interfaces, 11(4) (2019) 4507-4513.
[23] G. Chen, M. Jia, S. Zhang, Y. Tang, Z. Wan, Pool boiling enhancement of novel interconnected microchannels with reentrant cavities for high-power electronics cooling, International Journal of Heat and Mass Transfer, 156 (2020).
[24] J.Y.H. Goh, Y.M. Hung, M.K. Tan, Extraordinarily enhanced evaporation of water droplets on graphene-nanostructured coated surfaces, International Journal of Heat and Mass Transfer, 163 (2020).
[25] H. Moghadasi, H. Saffari, Experimental study of nucleate pool boiling heat transfer improvement utilizing micro/nanoparticles porous coating on copper surfaces, International Journal of Mechanical Sciences, 196 (2021).
[26] C. Park, T. Kim, Y.-I. Kim, A. Aldalbahi, M. Rafe Hatshan, S. An, S.S. Yoon, Pool boiling enhancement using hierarchically structured ZnO nanowires grown via electrospraying and chemical bath deposition, Applied Thermal Engineering, 187 (2021).
[27] Y. Zhang, X. Ma, Z. Zhu, L. Duan, J. Wei, Critical heat flux prediction model of pool boiling heat transfer on the micro-pillar surfaces, Case Studies in Thermal Engineering, 28 (2021).
[28] R.N. Wenzel, RESISTANCE OF SOLID SURFACES TO WETTING BY WATER, Industrial & Engineering Chemistry, 28(8) (1936) 988-994.
[29] D.E. Kim, S.C. Park, D.I. Yu, M.H. Kim, H.S. Ahn, Enhanced critical heat flux by capillary driven

liquid flow on the well-designed surface, Applied Physics Letters, 107(2) (2015).
[30] H. Kim, H.S. Ahn, H.J. Kwak, M.H. Kim, D.E. Kim, Boiling crisis controlled by capillary pumping and viscous friction: Liquid penetration length and dry spot diameter, Applied Physics Letters, 109(24) (2016).
[31] G. Bamorovat Abadi, M. Bahrami, A general form of capillary rise equation in micro-grooves, Sci Rep, 10(1) (2020) 19709.
[32] J. Li, G. Zhu, D. Kang, W. Fu, Y. Zhao, N. Miljkovic, Endoscopic Visualization of Contact Line Dynamics during Pool Boiling on Capillary‐Activated Copper Microchannels, Advanced Functional Materials, 31(4) (2020).
[33] C. Zhang, F. Yu, X. Li, Y. Chen, Gravity–capillary evaporation regimes in microgrooves, AIChE Journal, 65(3) (2018) 1119-1125.
[34] R. Wang, K. Jakhar, D.S. Antao, Unified Modeling Framework for Thin-Film Evaporation from Micropillar Arrays Capturing Local Interfacial Effects, Langmuir, 35(40) (2019) 12927-12935.
[35] R. Xiao, R. Enright, E.N. Wang, Prediction and optimization of liquid propagation in micropillar arrays, Langmuir, 26(19) (2010) 15070-15075.
[36] R. Xiao, E.N. Wang, Microscale liquid dynamics and the effect on macroscale propagation in pillar arrays, Langmuir, 27(17) (2011) 10360-10364.
[37] S.J. Kim, M.-W. Moon, K.-R. Lee, D.-Y. Lee, Y.S. Chang, H.-Y. Kim, Liquid spreading on superhydrophilic micropillar arrays, Journal of Fluid Mechanics, 680 (2011) 477-487.
[38] S.J. Kim, J. Kim, M.-W. Moon, K.-R. Lee, H.-Y. Kim, Experimental study of drop spreading on textured superhydrophilic surfaces, Physics of Fluids, 25(9) (2013).
[39] M.H. Alhosani, T. Zhang, Dynamics of Microscale Liquid Propagation in Micropillar Arrays, Langmuir, 33(26) (2017) 6620-6629.
[40] J. Kim, M.-W. Moon, H.-Y. Kim, Capillary rise in superhydrophilic rough channels, Physics of Fluids, 32(3) (2020).
[41] S. Ravi, R. Dharmarajan, S. Moghaddam, Measurement of Capillary Radius and Contact Angle within Porous Media, Langmuir, 31(47) (2015) 12954-12959.
[42] S.R. Krishnan, J. Bal, S.A. Putnam, A simple analytic model for predicting the wicking velocity in micropillar arrays, Sci Rep, 9(1) (2019) 20074.
[43] S. Ravi, D. Horner, S. Moghaddam, A novel method for characterization of liquid transport through micro-wicking arrays, Microfluidics and Nanofluidics, 17(2) (2013) 349-357.
[44] B. Dai, K. Li, L. Shi, X. Wan, X. Liu, F. Zhang, L. Jiang, S. Wang, Bioinspired Janus Textile with Conical Micropores for Human Body Moisture and Thermal Management, Adv Mater, 31(41) (2019) e1904113.
[45] S. Poudel, A. Zou, S.C. Maroo, Evaporation Dynamics in Buried Nanochannels with Micropores, Langmuir, 36(27) (2020) 7801-7807.
[46] G. Chen, D. Fan, S. Zhang, Y. Sun, G. Zhong, Z. Wang, Z. Wan, Y. Tang, Wicking capability evaluation of multilayer composite micromesh wicks for ultrathin two-phase heat transfer devices, Renewable Energy, 163 (2021) 921-929.
[47] D.I. Shim, G. Choi, N. Lee, T. Kim, B.S. Kim, H.H. Cho, Enhancement of Pool Boiling Heat Transfer Using Aligned Silicon Nanowire Arrays, ACS Appl Mater Interfaces, 9(20) (2017) 17595-17602.
[48] C.K. Wemp, V.P. Carey, Heat transport for evaporating droplets on superhydrophilic, thin, nanoporous layers, International Journal of Heat and Mass Transfer, 132 (2019) 34-51.

[49] H. Dai, R. Ding, M. Li, J. Huang, Y. Li, M. Trevor, Ordering Ag nanowire arrays by spontaneous spreading of volatile droplet on solid surface, Sci Rep, 4 (2014) 6742.
[50] X. Chen, J. Chen, X. Ouyang, Y. Song, R. Xu, P. Jiang, Water Droplet Spreading and Wicking on Nanostructured Surfaces, Langmuir, 33(27) (2017) 6701-6707.
[51] R. Xiao, K.-H. Chu, E.N. Wang, Multilayer liquid spreading on superhydrophilic nanostructured surfaces, Applied Physics Letters, 94(19) (2009).
[52] T.B. Nguyen, D. Liu, M.I. Kayes, B. Wang, N. Rashin, P.W. Leu, T. Tran, Critical heat flux enhancement in pool boiling through increased rewetting on nanopillar array surfaces, Sci Rep, 8(1) (2018) 4815.
[53] T.T. Mai, C.Q. Lai, H. Zheng, K. Balasubramanian, K.C. Leong, P.S. Lee, C. Lee, W.K. Choi, Dynamics of wicking in silicon nanopillars fabricated with interference lithography and metal-assisted chemical etching, Langmuir, 28(31) (2012) 11465-11471.
[54] B.S. Kim, H. Lee, S. Shin, G. Choi, H.H. Cho, Interfacial wicking dynamics and its impact on critical heat flux of boiling heat transfer, Applied Physics Letters, 105(19) (2014).
[55] J.G. Fan, Y.P. Zhao, Spreading of a water droplet on a vertically aligned Si nanorod array surface, Applied Physics Letters, 90(1) (2007).
[56] H.S. Ahn, G. Park, J. Kim, M.H. Kim, Wicking and spreading of water droplets on nanotubes, Langmuir, 28(5) (2012) 2614-2619.
[57] Y. Huang, Q. Chen, R. Wang, Visualization study on capillary-spreading behavior of liquid droplet in vertically aligned carbon nanotube array, International Journal of Heat and Mass Transfer, 120 (2018) 1055-1064.
[58] F.H. Kriel, R. Sedev, C. Priest, Capillary Filling of Nanoscale Channels and Surface Structure, Israel Journal of Chemistry, 54(11-12) (2014) 1519-1532.
[59] S. Poudel, A. Zou, S.C. Maroo, Droplet Evaporation on Porous Nanochannels for High Heat Flux Dissipation, ACS Appl Mater Interfaces, 13(1) (2021) 1853-1860.
[60] S. Poudel, A. Zou, S.C. Maroo, Wicking in Cross-Connected Buried Nanochannels, The Journal of Physical Chemistry C, 123(38) (2019) 23529-23534.
[61] J. Lee, Y. Suh, P.P. Dubey, M.T. Barako, Y. Won, Capillary Wicking in Hierarchically Textured Copper Nanowire Arrays, ACS Appl Mater Interfaces, 11(1) (2019) 1546-1554.
[62] A. Rokoni, D.O. Kim, Y. Sun, Micropattern-controlled wicking enhancement in hierarchical micro/nanostructures, Soft Matter, 15(32) (2019) 6518-6529.
[63] Z. Wang, J. Zhao, A. Bagal, E.C. Dandley, C.J. Oldham, T. Fang, G.N. Parsons, C.H. Chang, Wicking Enhancement in Three-Dimensional Hierarchical Nanostructures, Langmuir, 32(32) (2016) 8029-8033.
[64] D. Zheng, C.H. Choi, G. Sun, X. Zhao, Superwicking on Nanoporous Micropillared Surfaces, ACS Appl Mater Interfaces, 12(27) (2020) 30925-30931.
[65] A.S. Zuruzi, H.C. Gardner, A.J. Monkowski, N.C. MacDonald, Tailored nanostructured titania integrated on titanium micropillars with outstanding wicking properties, Lab Chip, 13(12) (2013) 2414-2418.
[66] M.H. Alhosani, H. Li, A.S. Alketbi, Q. Guan, A. Aili, T. Zhang, Enhanced Liquid Propagation and Wicking Along Nanostructured Porous Surfaces, Advanced Engineering Materials, 23(7) (2021).
[67] Y. Wang, Y. Lin, G. Yang, J. Wu, Flow Physics of Wicking into Woven Screens with Hybrid Micro-/Nanoporous Structures, Langmuir, 37(7) (2021) 2289-2297.
[68] J. Chun, C. Xu, Y. Zhang, Q. Li, R. Wen, X. Ma, Fast Capillary Wicking on Hierarchical Copper

662 Nanowired Surfaces with Interconnected V-Grooves: Implications for Thermal Management, ACS
663 Applied Nano Materials, 4(5) (2021) 5360-5371.
664 [69] Y. Im, C. Dietz, S.S. Lee, Y. Joshi, Flower-Like CuO Nanostructures for Enhanced Boiling,
665 Nanoscale and Microscale Thermophysical Engineering, 16(3) (2012) 145-153.
666 [70] S. Xie, M. Jiang, H. Kong, Q. Tong, J. Zhao, An experimental investigation on the pool boiling of
667 multi-orientated hierarchical structured surfaces, International Journal of Heat and Mass Transfer, 164
668 (2021).

669